

## Ozone Monitoring Instrument geolocation verification

M. Kroon,<sup>1</sup> M. R. Dobber,<sup>1</sup> R. Dirksen,<sup>1</sup> J. P. Veefkind,<sup>1</sup> G. H. J. van den Oord,<sup>1</sup>  
and P. F. Levelt<sup>1</sup>

Received 15 April 2007; revised 13 November 2007; accepted 28 December 2007; published 2 May 2008.

[1] Verification of the geolocation assigned to individual ground pixels as measured by the Ozone Monitoring Instrument (OMI) aboard the NASA EOS-Aura satellite was performed by comparing geophysical Earth surface details as observed in OMI false color images with the high-resolution continental outline vector map as provided by the Interactive Data Language (IDL) software tool from ITT Visual Information Solutions. The OMI false color images are generated from the OMI visible channel by integration over 20-nm-wide spectral bands of the Earth radiance intensity around 484 nm, 420 nm, and 360 nm wavelength per ground pixel. Proportional to the integrated intensity, we assign color values composed of CRT standard red, green, and blue to the OMI ground pixels. Earth surface details studied are mostly high-contrast coast lines where arid land or desert meets deep blue ocean. The IDL high-resolution vector map is based on the 1993 CIA World Database II Map with a 1-km accuracy. Our results indicate that the average OMI geolocation offset over the years 2005–2006 is 0.79 km in latitude and 0.29 km in longitude, with a standard deviation of 1.64 km in latitude and 2.04 km in longitude, respectively. Relative to the OMI nadir pixel size, one obtains mean displacements of  $\sim 6.1\%$  in latitude and  $\sim 1.2\%$  in longitude, with standard deviations of 12.6% and 7.9%, respectively. We conclude that the geolocation assigned to individual OMI ground pixels is sufficiently accurate to support scientific studies of atmospheric features as observed in OMI level 2 satellite data products, such as air quality issues on urban scales or volcanic eruptions and its plumes, that occur on spatial scales comparable to or smaller than OMI nadir pixels.

**Citation:** Kroon, M., M. R. Dobber, R. Dirksen, J. P. Veefkind, G. H. J. van den Oord, and P. F. Levelt (2008), Ozone Monitoring Instrument geolocation verification, *J. Geophys. Res.*, 113, D15S12, doi:10.1029/2007JD008821.

### 1. Introduction

[2] The Dutch-Finnish Ozone Monitoring Instrument (OMI) [Levelt, 2002; Levelt *et al.*, 2006a, 2006b] aboard the NASA EOS-Aura satellite [Schoeberl *et al.*, 2006] is a compact, nadir viewing, wide swath, ultraviolet-visible (UV/VIS), push-broom type imaging spectrometer that provides daily global coverage at moderate spatial and high spectral resolution. EOS-Aura was launched on 15 July 2004 into a sun-synchronous orbit at 705 km altitude with an ascending node local equator-crossing time roughly at 13:45. During the dayside portion of the orbit, the OMI instrument measures the Earth radiance with a moderate spatial and high spectral resolution. Near the northern hemisphere terminator OMI measures the Solar irradiance at high spectral resolution once per day. The ratio of Earth radiance and solar irradiance is the Earth reflectance from which atmospheric satellite data products, such as total column trace gas concentrations, clouds and aerosols physical properties, and surface UV irradiance levels are calculated.

[3] The OMI measurement principle is discussed in the IEEE Special Issue on the EOS-Aura mission [Dobber *et al.*, 2006; Levelt *et al.*, 2006a] and the OMI calibration status is discussed in this issue [Dobber *et al.*, 2008]. The instantaneous field of view of the nadir pointing telescope of OMI amounts to  $115^\circ$  oriented perpendicular to the flight direction of the EOS-Aura satellite. The main observation modes for OMI are the ‘global’ measurement mode, the ‘spatial zoom-in’ measurement mode and the ‘spectral zoom-in’ measurement mode [Dobber *et al.*, 2006] in which the CCD pixels are binned on the CCD chip in the spatial and/or spectral direction with different binning factors. Here we limit the discussion to the observations in the ‘global’ measurement mode. From the position and altitude of the EOS-Aura polar orbit, the instantaneous field of view provides OMI with a ground swath of 2600 km wide, which in the nominal ‘global’ observation mode is distributed over 60 individual ground pixels. In this mode the OMI instrument achieves complete daily global coverage of the sunlit portion of the Earth with the moderate spatial resolution of roughly  $13 \text{ km} \times 24 \text{ km}$  (along  $\times$  across track) at nadir. This relatively small nadir ground pixel size, or nadir ground sample distance, enables OMI to look “in between” the clouds, giving better reach into the troposphere for

<sup>1</sup>Royal Netherlands Meteorological Institute, De Bilt, Netherlands.

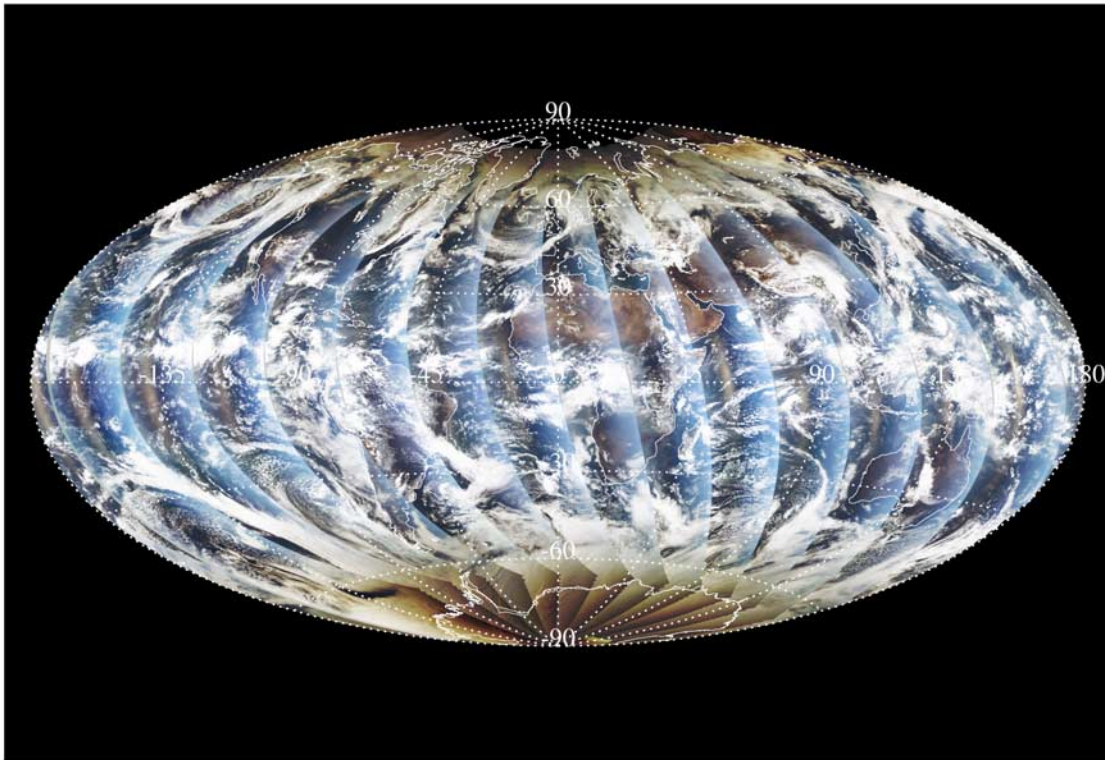


**Figure 1.** A single day of OMI R G B data comprising of the dayside portion of roughly 15 polar orbits [1176–1190] of EOS-Aura as captured on 4 October 2004 plotted in Hammer-Aitoff projection style. Plotting is limited to solar zenith angles smaller than 84 degrees to highlight the brightly lit Antarctic continent. This OMI false color image reveals the observation of the oceans, the continents, the poles, clouds, weather systems, and OMI daily global coverage. Brighter colors of larger pixels indicate outer OMI swath observations under extreme viewing angles where Rayleigh scattering contributes more. Solid white lines are used to indicate continental contours. Dashed white lines indicate the degrees of latitude and longitude.

retrieving tropospheric composition information than other UV-VIS backscatter instruments flown to date.

[4] On the basis of the elevation and azimuth angles as calibrated on-ground for each OMI ground pixel line-of-sight, the time of measurement and the EOS-Aura spacecraft ephemeris and attitude data provided by the NASA Goddard Space Flight Center Flight Dynamics Team, the OMI level 0-1B data processing software using the SDP Toolkit [Noerdlinger, 1995] calculates the geolocation of the center of each OMI ground pixel expressed in latitude and longitude. To support scientific studies of atmospheric composition features as observed from OMI level 2 ‘global’ satellite data products on trace gases and aerosols that occur on spatial scales comparable to or even smaller than the smallest spatial scales achievable by the OMI observations, one must verify that the geolocation assigned to the measured OMI ground pixels is sufficiently accurate for this purpose. Otherwise these features, which are mostly tropospheric events such as industrial pollution plumes, urban air pollution plumes, volcanic plumes, dust storms and biomass burning plumes, are artificially displaced with respect to their actual sources at the surface.

[5] In this paper we report on the verification of the OMI ground pixel geolocation by OMI false color imagery where we have employed the OMI radiance spectral data to display

geophysical Earth surface details, such as coast lines. By comparing such details by eye with their geographical position in the high resolution continental outline vector map as provided by IDL, which is based on the 1993 CIA World Database II Map (visit the following links for information: <http://geography.about.com/library/cia/blcindex.htm>, <https://www.cia.gov/cia/publications/mapspub/193.shtml>, [http://www.ngdc.noaa.gov/seg/cdroms/ged\\_iib/datasets/b14/mw.htm](http://www.ngdc.noaa.gov/seg/cdroms/ged_iib/datasets/b14/mw.htm)) (hereinafter referred to as WDBII sites), the OMI ground pixel geolocation accuracy can be quantified. A paper by Dobber *et al.* [2008] describing the validation of other OMI Level 1B data parameters can be found in this special section.

## 2. OMI False Color Images

[6] OMI false color images are generated by spectral band integration of the OMI level 1B Earth radiance intensity as recorded by the instrument’s visible channel. This ‘VIS’ channel has a spectral range of 349 nm to 504 nm, ranging from UV radiation invisible to the naked human eye to blue light. The Earth radiance intensity is integrated over three different wavelengths bands, where we use [474–494 nm] for ‘red’ or ‘R’, [410–430 nm] for ‘green’ or ‘G’, and [350–370 nm] for ‘blue’ or ‘B’, respectively. The

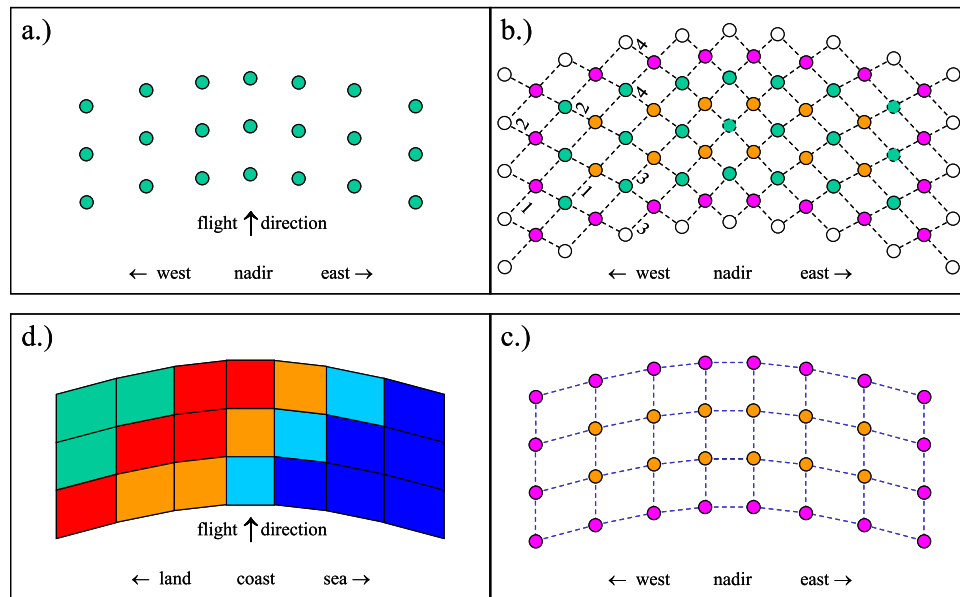


**Figure 2.** Constructing OMI ground pixel corner coordinates from center coordinates. (a) Read the center coordinates of subsequent swaths, here depicted by the green dots in a simplified manner and with reduced number of pixels. (b) Calculate the average pixel positions between center pixels rendering the orange dots. Perform linear extrapolation at east and west swath edge; that is, extend lines marked 1 and 2 and determine crossing points rendering the white and purple dots at the east and west swath edge. Perform linear extrapolation of North and South swath edge; that is, extend lines marked 3 and 4 and determine crossing points, rendering the white and purple dots at the North and South swath edge. (c) Define corner coordinates by connecting the purple and orange dots with “horizontal” (across track) and “vertical” (along track) blue colored dashed lines. (d) OMI false color image are obtained by uniformly filling each box with the respective R G B color value, here exemplified with land, coast, and sea.

histogram distributions of the integrated intensities encountered over one single orbit are subsequently histogram equalized per color channel over the range 0 to 255, the standard range of an 8 bit color scale, to enhance contrast. Plotting the color composed of the R G B values as a function of the pixel position (geolocation) yields OMI false color images of which various examples are shown throughout this document.

[7] Figure 1 depicts an example of a single day of OMI data as captured on 4 October 2004 revealing the oceans, the continents, clouds, sun glint, weather systems, a brightly lit South Pole and the North Pole covered in darkness, and OMI daily global coverage. The calculation of the size and shape of OMI ground pixels is described in the next section. For the purpose of this paper, being geolocation verification, we did not correct the OMI radiance observations for the presence of the Earth’s atmosphere in between the OMI satellite instrument and the Earth’s surface; that is, we do not try to obtain surface reflectivity data by correcting the OMI radiance observations for trace gas absorption and the presence of aerosols and clouds. However, when assigning geolocation coordinates to OMI ground pixels by the level 0-1B processor, the optical refractive index of the Earth’s atmosphere is taken into account. Although OMI is designed as an UV-VIS push broom type imaging spectrometer, the obtained OMI false color images are realistic representations of the Earth as seen in the visible channel of

dedicated high spatial resolution imaging satellite instruments such as MODIS aboard EOS-Aqua and EOS-Terra, albeit at a much poorer spatial resolution and at different wavelengths. This observation can be explained (1) from the dependence of the albedo as a function of wavelength of the various Earth surfaces such as land, ocean, and snow and ice, and (2) from the use of histogram equalization techniques.

[8] From the GOME albedo map [Koelemeijer and Stammes, 1999] one learns that the albedo of the deep ocean as a function of wavelength between 250 nm and 800 nm is a continuously decreasing function. For non-vegetated land surfaces such as deserts, the albedo is a continuously increasing function in this range. In essence, the spectral signature of land or sea in the wavelength range as captured by OMI is the same as in the region of human visual perception, explaining the natural appearance of the OMI false color images of the Earth. Please note that the OMI wavelengths associated with R G B are shifted considerably with respect to the standard definition of the R G B colors for CRT television, where  $R = \sim 610$  nm,  $G = \sim 545$  nm and  $B = \sim 463$  nm, depending on the choice of the particular cathodoluminescent phosphors [Shea, 1998]. (For an online version of this paper presenting an overview of the history and principles of cathodoluminescent phosphors please visit <http://www.electrochem.org/dl/interface/sum/sum98/IF6-98-Pages24-27.pdf>. For an elaborate overview

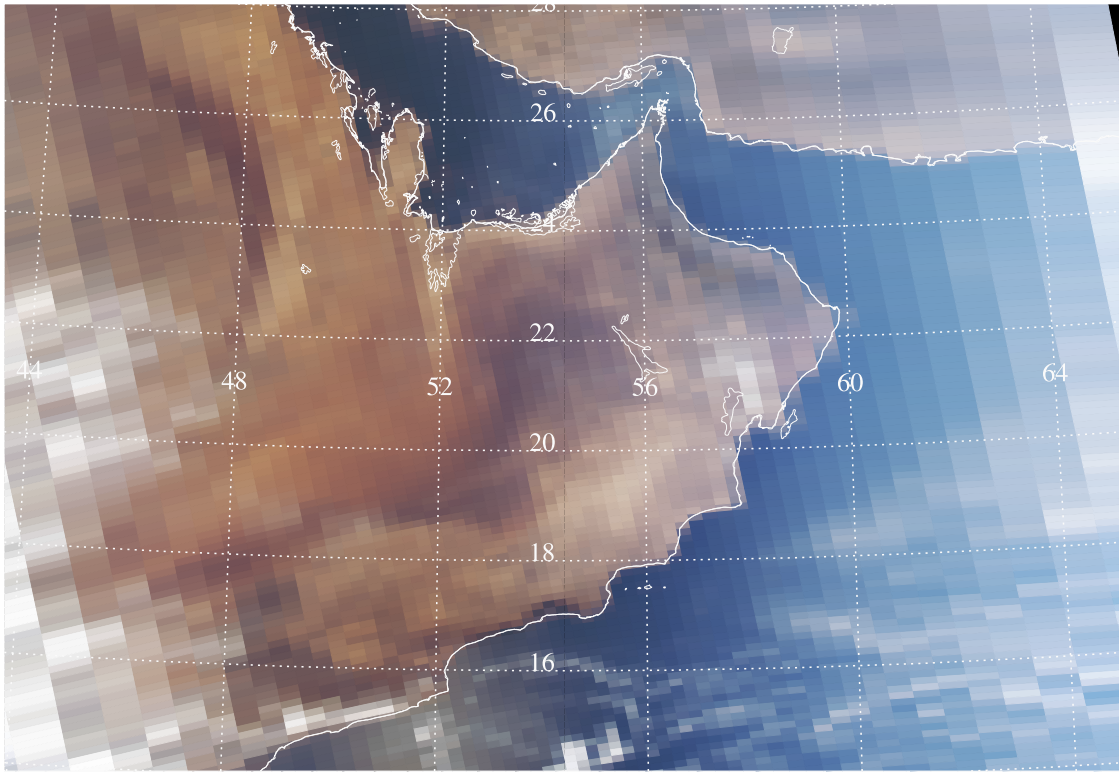


**Figure 3.** OMI false color image of EOS-Aura orbit 1152 recorded on 3 October 2004 and plotted in Hammer-Aitoff projection style, depicting a close-up of the southeast portion of the Arabian peninsula, revealing the size of individual OMI ground pixels and demonstrating the spatial resolving power of OMI in the nominal “global” observation mode. The high-resolution vector map is drawn in white, and OMI R G B data are plotted underneath. Note the sharp contrast between land and sea, in color and brightness. Note the surface structures of the desert caused by different mineral compositions of the soil. The orange feature at [20°N, 50°E] is most probably a dust storm.

of available cathodoluminescent phosphors please visit [http://en.wikipedia.org/wiki/Phosphor#Cathode\\_ray\\_tubes.](http://en.wikipedia.org/wiki/Phosphor#Cathode_ray_tubes.))

[9] Image enhancement by histogram equalization is a useful technique for enhancing low-contrast images [Acharya and Ray, 2005; Russ, 2002]. The resulting image color histogram is approximately uniform which has the effect of enhancing the dark areas and reducing the bright areas in an image. Here the use of histogram equalization removes the need for an accurate normalization of the three wavelength channels, and it removes the need for normalizing the Earth radiance to the Solar irradiance, which over the selected wavelength bands is approximately a constant.

### 3. OMI Corner Coordinates

[10] In the nominal ‘global’ observation mode, the OMI instantaneous field of view of 115° is equally divided into 60 pixels, yielding just below 2° of cross track field of view coverage per pixel. In combination with the OMI integration time of two seconds this yields the moderate spatial resolution of roughly 13 km × 24 km (along × across track) at nadir. Owing to the Earth’s curvature the outer pixels of the OMI swath cover a much larger ground track than nadir pixels do, up to 120 km cross track. For visualization, validation and scientific purposes of OMI level 1B and level 2 data products one would like to have the exact shape

and size of the OMI ground pixels at hand. However, at present and for the foreseeable future, the OMI level 0-1B data processor does not provide this information (1) because the true OMI instantaneous field of view is a complicated function of various optical instrument properties that are not accurately known and (2) because level 1B data users may opt for different choices of how much of the observed radiance energy they define to be contained in their ground pixel definition. For this reason the choice was made within the OMI project to let the OMI level 1B data processor provide only the latitude and longitude of the center of each ground pixel that is accurately calibrated on-ground. Hence an off-line computation scheme is required to derive such coordinates.

[11] Here we present a simple scheme to derive four corner coordinates of rectangular OMI ground pixels from the latitude and longitude values of the OMI ground pixel centers as assigned to the individual OMI ground pixels. The process is schematically shown in Figure 2 and relies on simple linear interpolations and extrapolations of the pixel center coordinates. Interpolations yield the average pixel positions between center pixels. Extrapolations yield the approximate size of west and east pixels and the pixels at the orbit terminators. Figure 3 shows the OMI false color image of EOS-Aura orbit 1152 recorded on 3 October 2004 depicting a close-up of the southeast portion of the Arabian

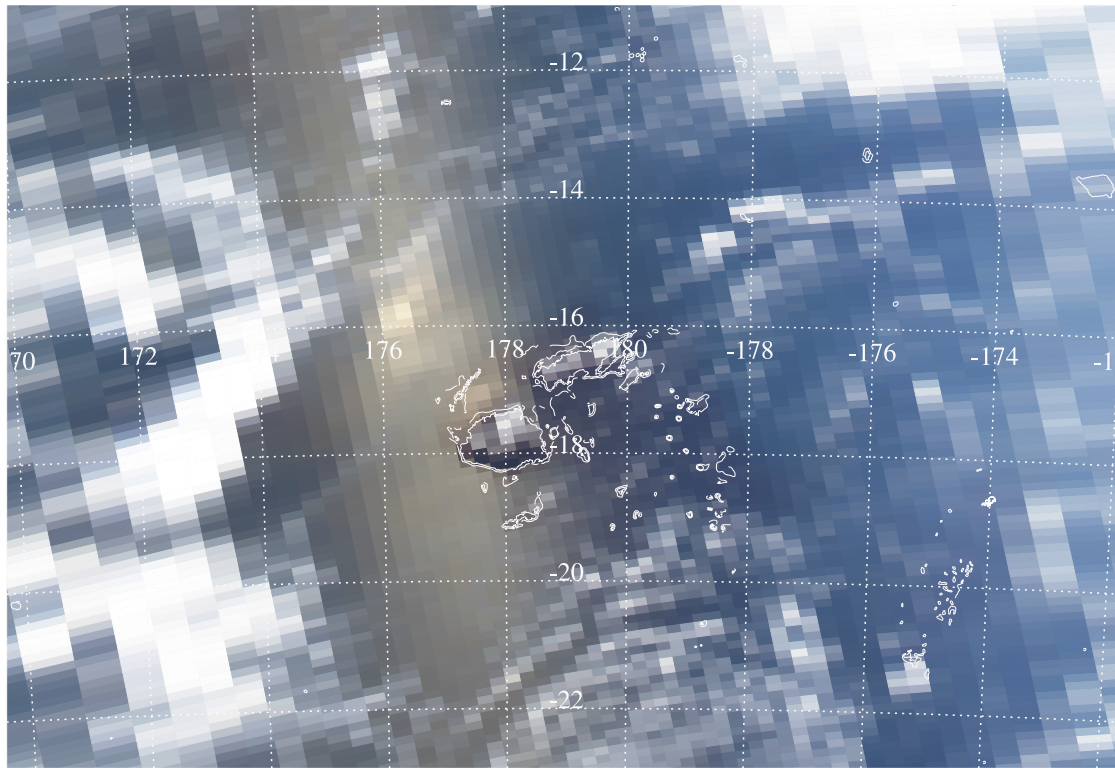


**Figure 4.** OMI false color image of EOS-Aura orbit 2953 recorded on 3 February 2005 and plotted in Hammer-Aitoff projection style, depicting the Fiji Islands in Sun glint. Note the presence of the date line right over the Fiji Islands causing no plotting problems when taking proper precautions to avoid date line plotting problems. Note the size of OMI ground pixels increasing from nadir toward the swathe edge and the observation of cloud structures. Also note the small but bright sun glint spot near [16°S,176°E], indicative of a calm sea surface.

peninsula. Here land, ocean and clouds are represented in their pseudo-natural colors. The image reveals surface structures in the main land desert caused by different mineral compositions of the soil. Note the sharp contrast between land and sea in this picture, in both vivid color and in brightness. The sun glint actually inverts the contrast, rendering a sea brighter than the land. Figure 3 reveals the size of individual OMI ground pixels obtained when following the simple scheme as presented here and demonstrates the spatial resolving power of OMI in the nominal ‘global’ observation mode.

[12] Various problems occur when performing interpolations and extrapolations of the spatial center positions of OMI ground pixels on the globe, caused by the poles and the date line. When crossing the poles, the center longitude of the OMI ground pixels changes considerably whereas the center latitude of these pixels hardly changes. Averaging and extrapolations may render values that yield errors when plotted hence ground pixels containing the poles are not plotted. When crossing the date line from east to west, the magnitude of the center longitude changes from  $-180^\circ$  to  $+180^\circ$  rendering zero values for the interpolated longitude. To deal with the date line one may search for the location of the sign change of the longitude over the OMI swath and add  $360^\circ$  to the values west of the sign change, thereby removing the sign change but yielding values larger than  $+180^\circ$ . Most plotting programs, however, assign appropriate

values between  $-180^\circ$  and  $+180^\circ$  to any longitude value. Figure 4 shows the OMI false color image of EOS-Aura orbit 2953 recorded on 3 February 2005, depicting the Fiji Islands in Sun glint. Note the presence of the date line right over the Fiji Islands causing no plotting problems when taking proper precautions.

[13] The center coordinates of OMI ground pixels are calculated from the center angular direction of the field of view of that particular pixel. Already for a flat Earth approach this will yield pixel center coordinates which are not in the symmetrical center of that ground pixel but are positioned slightly toward nadir. The curvature of the Earth will add to this effect which will be more pronounced for the ground pixels toward the swathe edge. Both mentioned mechanisms will have little to none affect on the nadir pixels which are predominantly used in these studies. On average when using pixels to the left and right hand side of the nadir position this effect will most likely average out.

#### 4. Geolocation Verification

[14] Verification of the geolocation assigned to individual OMI ground pixels was performed by comparing geophysical Earth surface details as observed from OMI false color images with the high-resolution continental outline vector map as provided by IDL. Most suitable geophysical Earth surface details are the coast lines between desert land and deep ocean, as shown in Figure 3, and small isolated barren

islands. Also, coast lines and small islands positioned in the sun glint spot are of use, as shown in Figure 4. Despite using image enhancement techniques such as histogram equalization, other features such as the coast lines of vegetated land and shallow sea simply do not have sufficient contrast for this purpose.

[15] IDL supports two different data sets that contain continent outlines and other geographical and political boundaries. The default data set is a low-resolution continental outline database. The high-resolution continental outline database was adapted from the 1993 CIA World Map database by Thomas Oetli of the Swiss Meteorological Institute. Data points in the high-resolution database are approximately one kilometer apart (IDL help, <https://www.itvis.com/idl/docs/pdfs/using.pdf>). The 1993 CIA world map database, or World Data Bank II (see WDBII sites), represent perhaps the first globally consistent vector databases of coastlines, roads, inland water bodies, rivers, and populated places. These data were originally digitized by the U.S. Central Intelligence Agency (CIA) from operational navigation charts and other source maps during the late 1970s and early 1980s [Dooley, 2005]. The World Bank II original data set is a series of COBOL records, specifying 5,719,617 individual vectors, which occupies about 130 megabytes of disk space. According to an intermediate processing of these data for the Micro World Data Bank II, the base map scales used ranged from 1:750,000 to 1:4,000,000 with a nominal scale of 1:3,000,000 (Pospeschil Micro World Data Bank II, [http://www.ngdc.noaa.gov/seg/cdroms/ged\\_iib/datasets/b14/mw.htm](http://www.ngdc.noaa.gov/seg/cdroms/ged_iib/datasets/b14/mw.htm)). The Pospeschil reference states that the "point coordinates are rounded to 1 minute in latitude and longitude" which puts the point coordinates accuracy at  $\pm 0.9$  km calculated from  $30 \text{ arcsec} \times \sim 30 \text{ m/arcsec}$ . On the basis of the USGS map accuracy standards (<http://erg.usgs.gov/isb/pubs/factsheets/fs17199.pdf>) a 1:3,000,000 scale map has a horizontal accuracy of 1.525 km for well-defined points; that is, 90% of the points are within a circle with a radius of 1.525 km.

[16] In practice, geolocation verification starts with plotting a number of OMI R G B orbits on a global map and examine the picture by eye for an appropriate scene. Our home-built plotting software allows us to zoom in on a particularly favorable region of interest to perform geolocation verification and optimize image brightness. In Figure 3 an example is shown where a close-up of the south east portion of the Arabic peninsula is depicted. With the IDL high-resolution vector map plotted on top of the OMI false color image, one already obtains a coarse idea of the accuracy of the geolocation assigned to individual OMI ground pixels. In our home-built plotting software the IDL high-resolution vector map can be shifted in longitudinal and latitudinal direction over the OMI false color image in steps of  $1^\circ/100$  until an optimal correspondence is obtained, determined by visual inspection, meaning that the positioning of the vector map is in agreement with the observed ground pixel colors.

[17] In principle one could not perform geolocation verification more accurately than the spatial size of the OMI ground pixel sizes involved. However, the color of desert coast line ground pixels is composed of two very different contributions as these ground pixels cover both

'yellow' land and 'blue' ocean with a certain ratio, rendering a mixed color between the two extremes. Examples of such pixels are displayed in Figure 3 along the coast line of Oman where ground pixel color smoothly changes from land to ocean, from yellow to blue. Under such conditions geolocation verification is achieved by positioning the IDL high-resolution vector map such that the location of the coast line is in agreement with the colors of the ground pixel involved; purely land and purely ocean on either side of the coast line, and pixels mixed by fraction underneath the coast line. In the particular example of Figure 3 one also encounters many locations where the coast line happens to run parallel or orthogonal to the OMI swath and, on occasion falls in between two subsequent OMI along or across track pixels as observed from the vivid ground pixel colors on either side of the coast line. In those cases comparisons with the high-resolution vector map are the most accurate. Also note the sun glint at the south coast of Yemen, inverting the land-sea contrast transition. In practice, the Middle East region, Baja California and the coast lines of the countries around the Arabic Sea, the Red Sea, and the Mediterranean Sea provide the scenes with highest contrast. Small islands filling only a few OMI pixels such as Socotra, Cyprus, Crete, the Canary Islands and the Cape Verde Islands provide scenes with the highest accuracy for verification.

[18] Geolocation verification targets are limited on purpose to lie in the area between  $40^\circ\text{S}$  and  $40^\circ\text{N}$  to be able to separate along track and across track misalignments of the OMI orbits. Hence no compensation was needed of the obtained longitude shifts for the convergence of the lines of longitude away from the equator, i.e., a cosine latitude adjustment. Furthermore, we predominantly use the 20 OMI ground pixels around nadir for this purpose rendering the highest contrast. The 20 more westward or eastward ground pixels of the OMI swath soon become too large to resolve coast line features and their contrast is reduced by the increasing contribution of Rayleigh scattering.

[19] While browsing through the database of more than two and a half years of OMI false color images, in search of high-contrast features suitable for geolocation verification, one encounters interesting recordings of the Earth as 'seen' by the OMI instrument. Examples of surface features are; ocean surface sun glint for flat and wavy ocean surfaces, desert to ocean coast lines, desert soil features over Saudi Arabia, snow covered land coast lines, Greenland fjords, sea ice sheets around Antarctica, lake Victoria, the vegetated Nile river banks, the solar eclipse of 29 March 2006, the light blue lake Gara Bogaz, and more. Atmospheric features are; global cloud coverage, tropical storms, the eyes of hurricane Katrina (August 2005) and Typhoon Prapiroon (July 2006), dust storms from Africa reaching South America, dust storms from the Gobi desert covering Asia, biomass burning in Africa, south east Asia, Australia and recently over Greece, and more. Making movies of daily OMI false color globes sets all this in motion and reveals its dynamics.

## 5. Statistical Results

[20] Table 1 and Figure 5 present the statistical results of OMI geolocation verification grouped per month for the

**Table 1.** Results of OMI Geolocation Verification for the Years 2005–2006<sup>a</sup>

	$\langle \text{Lat} \rangle_w$	$\sigma(\text{Lat})_w$	$\langle \text{Lon} \rangle_w$	$\sigma(\text{Lon})_w$	Number of Scenes
Jan 2005	1.22	2.22	0.67	3.41	15
Feb 2005	1.28	1.92	-0.15	3.49	15
March 2005	0.90	1.88	-0.41	2.73	19
April 2005	1.18	2.59	-0.22	2.38	15
May 2005	1.17	2.25	0.15	3.11	15
June 2005	0.64	1.76	0.28	1.54	16
July 2005	0.56	1.92	-0.32	2.44	14
Aug 2005	0.48	1.66	0.07	2.43	15
Sept 2005	0.38	1.94	-0.07	1.70	16
Oct 2005	1.01	1.83	0.14	2.18	16
Nov 2005	0.75	1.77	0.49	1.86	16
Dec 2005	1.02	2.07	0.89	2.79	15
Jan 2006	0.73	1.52	0.81	1.70	15
Feb 2006	0.49	2.00	0.37	1.91	15
March 2006	0.42	1.51	0.37	2.38	18
April 2006	0.70	1.35	0.69	1.56	16
May 2006	0.87	1.26	0.16	1.50	14
June 2006	0.35	1.55	0.14	2.18	16
July 2006	0.75	1.62	0.07	2.09	16
Aug 2006	0.66	0.89	0.28	1.18	16
Sept 2006	0.47	0.74	0.15	1.02	15
Oct 2006	0.93	1.24	0.48	0.84	14
Nov 2006	0.87	0.98	0.67	0.92	15
Dec 2006	1.25	0.89	0.56	1.62	14
Average	0.79	1.64	0.26	2.04	15.5
Min	0.35	0.74	-0.04	0.85	14
Max	1.28	2.59	0.67	3.52	19
$\sigma$	0.29	0.47	0.35	0.74	1.18

<sup>a</sup>The symbol ' $\langle \rangle_w$ ' denotes the statistical mean of the weighed displacement, and the symbol ' $\sigma(\langle \rangle_w$ ' denotes the standard deviation, in latitude ('Lat') and longitude ('Lon'). Per month the number of scenes analyses is reported in the last column. Displacement numbers are reported in kilometers. Please consult the text of section 5 numbers were obtained.

years 2005–2006. Per month more than 15 scenes were analyzed on average. For each of these scenes the displacement of the IDL high-resolution vector map needed to obtain optimal correspondence with features observed from the OMI R G B image, following the procedure described in the previous section, was recorded, expressed in degrees/100. Furthermore, per comparison an uncertainly value was recorded for the latitudinal and longitudinal displacement separately, denoted as  $\Delta_{lat}$  and  $\Delta_{lon}$  respectively, expressing in degrees/100 the ranges in latitude and longitude over which the position of optimal correspondence can be varied for the comparison to be judged by eye as acceptable. From these uncertainly values a weighing factor was obtained, as  $1/\Delta_{lat}$  and  $1/\Delta_{lon}$ , with which the values for the optimal latitudinal and longitudinal displacement are weighed. These weighing factor express the accuracy of the obtained optimal correspondence; smaller ranges will yield larger weighing factors. In this way the better defined scenes weigh more in the resulting average displacement than less well defined scenes do. For example, for sharply defined scenes such as depicted in Figure 3, these ranges can be as small as  $2^\circ/100$  leading to a weighing factor of 50 for this scene. Other less well defined scenes will yield ranges typically of  $10^\circ/100$  leading to a weighing factor of 10. Finally, per month the weighed statistical results expressed in degrees/100 are converted into distances in kilometers using an equatorial conversion factor of ( $40,000 \text{ km}/360^\circ =$ )  $\sim 111 \text{ km per degree}$ .

[21] Table 1 provides the weighed statistical mean and the weighed statistical standard deviation of the latitudinal and longitudinal displacement, expressed in kilometers, per

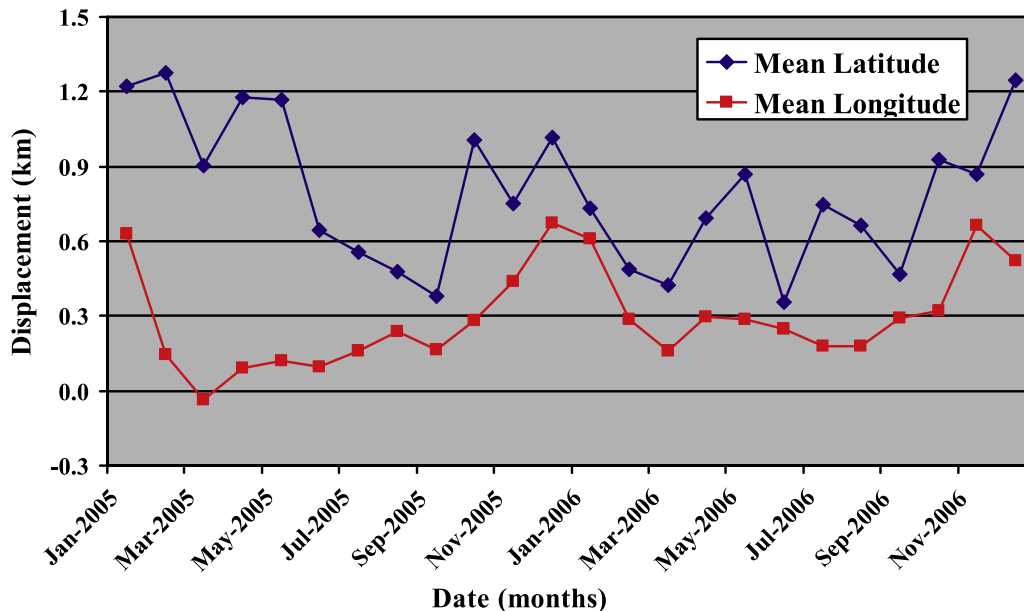


**Figure 5.** The weighed statistical results of OMI ground pixel geolocation verification for the years 2005–2006. Blue diamonds denote latitudinal displacements where red squares denote longitudinal displacements. Numbers are reported in kilometers. Averaged over these years, the weighed statistical mean deviation amounts to 0.79 km in latitude and 0.26 km in longitude, with weighed standard deviations of 1.64 and 2.04 km, respectively. Proving the presence of a seasonal signature in the monthly mean displacements is challenging given the large average standard deviations of 1.64 km in latitude and 2.04 km in longitude, respectively. Standard deviations per month are not plotted for clarity of the graph.

month for the years 2005–2006. Table 1 also provides the number of scenes analyzed per month. Please note that we also report the mean and the standard deviation over the years 2005–2006 for all statistical quantities presented. Averaged over these years, the mean of the monthly averaged weighed statistical deviation amounts to 0.79 km in latitude and 0.26 km in longitude, respectively. The mean of the monthly averaged weighed statistical standard deviation amounts to 1.64 km in latitude and 2.04 km in longitude, respectively. Relative to the OMI nadir pixel size one obtains mean displacements of  $\sim 6.1\%$  in latitude and  $\sim 1.2\%$  in longitude, with standard deviations of 12.6% and 7.9%, respectively.

[22] Figure 5 presents the numbers of Table 1 in a graphical manner. The latitudinal displacement shows a definite positive offset with a large variability around the mean. Taking into account the mean weighed standard deviation of 1.64 km the latitudinal displacement shows no clear seasonal signature. However, over the two years of analysis the latitudinal displacement first shows a negative trend and then, roughly after March 2006, shows a positive trend. The longitudinal displacement on the other hand shows a slow but steady positive trend over the years 2005–2006. Localized maxima occur around each turn of the year suggesting a seasonal effect.

## 6. Discussion

[23] In the analysis presented in this paper we have used a simple but effective scheme to obtain the four corner coordinates of rectangular pixels representing OMI ground pixels. More complicated calculation schemes require accurate knowledge of the spacecraft altitude, spacecraft velocity on the ground, the instantaneous field of view (IFOV) and point spread function (PSF) of the individual OMI instrument CCD pixels, and the schemes of photon accumulation integration times of the OMI CCD detectors. Here one also needs to take into account the sensitivity of the mentioned terms to the direction of polarization of the Earth radiance intensity and the effectiveness of the polarization scrambler aboard OMI. The true OMI ground pixel is obtained by a convolution of these complex terms. Furthermore, the main observation modes for OMI are the ‘global’ measurement mode, the spatial zoom-in measurement mode and the spectral zoom-in measurement mode [Dobber *et al.*, 2006] in which the CCD pixels are binned on the CCD chip in the spatial and/or spectral direction with different binning factors, which further complicates these calculations.

[24] At the 2007 OMI science team meeting the outcome of ray tracing calculations on OMI ground pixels were presented as photon (sensitivity) density patterns for various OMI ground pixel positions in the swath. From these distributions the shape and size of an OMI ground pixel can be obtained by choosing a threshold intensity level below which incoming light does not contribute significantly to the detected Earth radiance. By means of this threshold one decides where to place the pixel boundary. At a 10% threshold level the nadir OMI ground pixels were reported to be rectangles of approximately the nadir pixel size, however, with rounded corners. Here the rectangular approach certainly applies. Moving outward to the swath edge, this shape smoothly transform into elongated and

slightly curved rectangles ending in semicircles. These rectangles were not reported to become larger in the forward direction, just wider in the across track direction owing to the signal integration in the forward direction; the convolution of the small forward field of view with the signal integration curve. The simplest mathematical approach following the rectangle is the ellipse which was chosen primarily for its simple implementation in level-2 retrieval algorithms. However, the choice for this mathematical shape was already debated heavily as the ellipse did not match well with the reported intensity distributions for any swath position. In the geolocation verification studies presented in this paper nadir pixels are predominantly used for which we argue that the rectangular approach applies.

[25] The results presented in this paper have been obtained using the radiance signal of the OMI visible channel only. On the basis of the results obtained by the OMI in-flight calibration program and considering the design of the OMI optics the results presented here are qualitatively representative of the quality of the geolocation assignment to the OMI ground pixels in the UV-1 and UV-2 detection channels.

## 7. Conclusions

[26] Verification of the geolocation assigned to OMI ground pixels was performed for the years 2005–2006 by comparing geophysical Earth surface details as observed from OMI false color images, with a high-resolution vector map based on the 1993 CIA world map. Our results indicate that the average geolocation offset of OMI R G B data with respect to the 1993 CIA world map is less than 1 km in both latitude and longitude with no clear seasonal signature. We therefore conclude that the geolocation assigned to individual OMI ground pixels is sufficiently accurate to support scientific studies of those features as observed in OMI satellite data products that are of the spatial scale of the OMI nadir pixels or smaller. Examples are air quality issues on urban scales, industrial and urban outflow, volcanic plumes, biomass burning plumes and the highly detailed structure of the northern and southern hemisphere vortex edge breakup at the end of the ozone hole seasons.

[27] **Acknowledgments.** The Dutch-Finnish-built OMI instrument is part of the NASA EOS-Aura satellite payload. The OMI project is managed by NIVR and KNMI in the Netherlands. OMI R G B data were obtained from the KNMI OMI Trend Monitoring and In-Flight Calibration Facility (TMCF).

## References

- Acharya, T., and A. K. Ray (2005), *Image Processing: Principles and Applications*, Wiley-Intersci., Hoboken, N. J.
- Dobber, M. R., et al. (2006), Ozone Monitoring Instrument calibration, *IEEE Trans. Geosci. Remote Sens.*, 44(5), 1209–1238.
- Dobber, M. R., Q. Kleipool, R. Dirksen, P. F. Levelt, G. Jaross, S. Taylor, T. Kelly, and L. Flynn (2008), Validation of Ozone Monitoring Instrument level-1b data products, *J. Geophys. Res.*, doi:10.1029/2007JD008665, in press.
- Dooley, J. F., Jr. (2005), (Spatial Data Services & Mapping), An inventory and comparison of globally consistent geospatial databases and libraries, *Environ. and Nat. Resour. Working Pap. 19*, Food and Agric. Org., Rome. (Available at <http://www.fao.org/docrep/008/a0118e/a0118e00.htm>)
- Koelemeijer, R. B. A., and P. Stammes (1999), Effects of clouds on ozone column retrieval from GOME UV measurements, *J. Geophys. Res.*, 104, 8281–8294.

- Levelt, P. F. (Ed.) (2002), OMI algorithm theoretical basis document, vol. I, OMI instrument, level 0-1B processor, calibration & operations, *ATBD-OMI-01*, 50 pp., R. Neth. Meteorol. Inst. (KNMI), De Bilt, Netherlands. (Available at <http://www.knmi.nl/omi/research/documents/>)
- Levelt, P. F., E. Hilsenrath, G. W. Leppelmeier, G. H. J. van den Oord, P. K. Bhartia, J. Tamminen, J. F. de Haan, and J. P. Veefkind (2006), Science objectives of the Ozone Monitoring Instrument, *IEEE Trans. Geosci. Remote Sens.*, *44*(5), 1199–1208.
- Levelt, P. F., G. H. J. van den Oord, M. R. Dobber, A. Malkki, H. Visser, J. de Vries, P. Stammes, J. O. V. Lundell, and H. Saari (2006), The Ozone Monitoring Instrument, *IEEE Trans. Geosci. Remote Sens.*, *44*(5), 1093–1101.
- Noerdlinger, P. D. (1995), Theoretical basis of the SDP Toolkit Geolocation Package for the ECS project, technical paper, Hughes Appl. Inf. Syst., Landover, Md. (Available at <http://edhs1.gsfc.nasa.gov/waisdata/tns/pdf/tp4450202.pdf>)
- Russ, J. C. (2002), *The Image Processing Handbook*, 4th ed., CRC Press, Boca Raton, Fla.
- Schoeberl, M. R., et al. (2006), Overview of the EOS-Aura mission, *IEEE Trans. Geosci. Remote Sens.*, *44*(5), 1066–1074.
- Shea, L. E. (1998), Low-voltage cathodoluminescent phosphors: A 20-year chronology of low-voltage cathodoluminescence efficiency, report, *Electrochem. Soc. Interface*, *7*(2), 24–28.
- 
- R. Dirksen, M. R. Dobber, M. Kroon, P. F. Levelt, G. H. J. van den Oord, and J. P. Veefkind, Royal Netherlands Meteorological Institute, P.O. Box 201, NL-3730 AE De Bilt, Netherlands. (mark.kroon@knmi.nl)